J. Fluid Mech. (2010), *vol.* 658, *pp.* 383–408.
doi:10.1017/S0022112010001783

A numerical nonlinear analysis of two-dimensional ventilating entry of surface-piercing hydrofoils with effects of gravity

VIMAL VINAYAN† AND SPYROS A. KINNAS

Ocean Engineering Group, Department of Civil, Architectural and Environmental Engineering, University of Texas at Austin, Austin, TX 78712, USA

(Received 3 September 2009; revised 8 April 2010; accepted 9 April 2010; first published online 30 June 2010)

The presence of the free surface adds an element of difficulty to the development of numerical and theoretical methods for the performance prediction of surface-piercing hydrofoils. Existing methods of analysis for two-dimensional surface-piercing hydrofoils or blade sections of a surface-piercing propeller solve either a linear problem, assuming a thin section and ventilated surface along with linear free-surface boundary conditions, or a nonlinear problem in a self-similar setting. Both these approaches cannot be used when the effects of gravity are important, which is the case when a craft is operating at low speeds. A two-dimensional boundary-element-method-based numerical scheme is presented here that overcomes these drawbacks by solving the fully ventilated flow past a surface-piercing hydrofoil of finite dimensions and includes the whole gamut of nonlinear free-surface interactions. The unique aspect of the numerical scheme is that fully nonlinear boundary conditions are applied on the free surface which allows for the accurate modelling of the jet generated on the wetted boundary and the ventilated surface formed on the suction side as a result of the passage of the hydrofoil through the free surface. Moreover, the effects of gravity can be considered to take into account the influence of the Froude number. Ventilated-surface shapes predicted by the present scheme are compared with existing experimental results and are shown to be in good agreement.

Key words: computational methods

1. Introduction

Surface piercing or partially submerged propellers have emerged as one of the efficient systems of propulsion for high-speed crafts. The concept of having only a part of the propeller submerged during a cycle of revolution offers a rather unique set of advantages that gives better efficiency compared to conventional subcavitating or supercavitating submerged propellers. Some of the advantages that contribute towards a better propulsive efficiency and extended range of operation are (i) a considerable reduction in the appendage drag due to the absence of submerged components like shafts and struts, (ii) a reduction in the detrimental effects of cavitation as it is replaced by ventilation and (iii) the absence of diameter limitations imposed by draft and hull-clearance requirements. Despite these advantages, the partially submerged

† Email address for correspondence: vvinayan@mail.utexas.edu

propellers have problems like vibration of blades and low efficiency when the high-speed craft is operating at lower speeds. These require careful consideration during design.

The development of theoretical and numerical methods for the performance prediction of propellers is complicated. The presence of the free surface adds an element of difficulty in the case of surface-piercing propellers. There is a strong nonlinear interaction between the propeller and the free surface in the form of fast moving jets that are formed along the pressure side and elevation of the water surface. An add-on to the above nonlinear interaction is the effect of gravity, expressed in terms of the Froude number representing the relative importance of inertial fluid forces over gravitational forces.

Yim (1969, 1971, 1974) initiated the development of theoretical methods to predict the performance characteristics of surface-piercing propellers by assuming a two-dimensional flow field, which is obtained by unfolding the cylindrical surface containing the blade element at a certain radius. The two-dimensional flow field in essence consists of a layer of water, the thickness of which is equivalent to the distance travelled by the leading edge of the blade element along the helical line during one revolution. The blade element enters the layer at the top and exits through the bottom part. This approach was applied by Yim (1969, 1971, 1974) to develop a linear theory for the entry and exit of a thin hydrofoil and a base-vented symmetric wedge. Cox (1971) also considered a similar linearized problem but included the effects of gravity and made comparisons with experimental observations of the ventilated cavities formed as a result of the vertical entry of a wedge-shaped blade element. Wang (1977, 1979) applied the same approach as Yim (1969, 1971, 1974) to blade profiles with full ventilation and also extended the scheme for an oblique entry and exit. Another notable work based on linear theory is that of Terent'ev (1979). Common to all the above theoretical methods is the linearization of the blade and ventilated surfaces, assuming that both are thin, and the application of the linearized free-surface boundary conditions on the original undisturbed location of the free surface. Yim (1969, 1971, 1974), Wang (1977, 1979) and Terent'ev (1979) based their methods on an infinite Froude number (no gravity) approximation for the free surface, assuming that the duration of the entry-and-exit event is short and the velocity of entry is high. An exception to this is the method of Cox (1971), who considered an arbitrary entry speed and included the effects of gravity. Very few theoretical methods exist that take into account the full nonlinearity of the ventilating problem. Two notable works are those of Chekin (1989) and Faltinsen & Semenov (2008). Both the methods solved the ventilating entry of a semi-infinite flat plate within the precepts of self-similarity.

In terms of numerical methods, Savineau & Kinnas (1995) developed a method to solve the flow field around a fully ventilated two-dimensional surface-piercing blade section using a time-marching low-order boundary-element method (BEM). The important characteristics of the method are as follows: (i) the flow is solved with respect to a coordinate system that moves along with the section, (ii) the vertical velocity of entry is assumed to be sufficiently high for ventilation to start at the sharp leading edge of the section and form a ventilated surface along the suction side, (iii) an infinite Froude number is assumed and with this assumption, the free-surface boundary conditions are linearized and the effects of gravity neglected, (iv) the linearized free-surface boundary conditions are enforced using a 'negative'-image method.

The application of the above linear and nonlinear theories is limited to simple geometries in a gravity-free space. Moreover, the similarity solution method cannot be used for sections of finite chord length. Although the numerical method of Savineau

& Kinnas (1995) can be applied to sections of arbitrary shapes and finite dimensions, it is limited in application because of the negative-image treatment of the free surface. These shortcomings provide the motivation for this work, which is the development of a numerical method with the following features:

(*a*) Fully nonlinear free-surface boundary conditions.

(*b*) Effects of gravity included: the parameter determining the influence of gravity on the performance characteristics of a surface-piercing propeller is the Froude number, defined as $F_n = nD/\sqrt{gD}$, where n is the rotational speed of the propeller, g the acceleration due to gravity and D the diameter of the propeller.

It is well known from the experimental results of Shiba (1953) and Olofsson (1996) that it is permissible to use zero-gravity theory in predicting the performance characteristics of surface-piercing propellers when $F_n > 3$. This limit, however, does not cover the entire range of operation of the surface-piercing propeller. Even with the fully ventilated blades, the propeller can operate at Froude numbers less than 3, which occur at low craft speeds. The experimental results of Olofsson (1996) show that the effect of gravity cannot be neglected for these cases as it is seen to affect not only the force distribution but also the shape of the ventilated surface. Thus, it is important that along with the nonlinearity of the free surface, effects of gravity be considered to cover the entire range of operation of the propeller.

(*c*) Ventilating entry of arbitrarily shaped hydrofoils of finite dimensions: the emphasis here is on predicting the ventilating flow during the critical entry phase.

In the following sections, the physical assumptions, mathematical formulation and numerical solution method will be presented. The experimental results of Cox (1971) are chosen for comparison and validation of the numerical scheme described here.

2. Physical assumptions

The physical assumptions made in the modelling of the ventilating problem are as follows:

(*a*) The flow is considered to be inviscid and irrotational, assuming that the speed of entry is high enough to limit the effects of viscosity to a thin boundary layer.

(*b*) The dynamics of the surrounding air is neglected except for maintaining the ventilated surface/free surface at a constant pressure – in the case of ventilation, the surface is maintained at atmospheric pressure.

(*c*) The fluid is incompressible, assuming that the speed of entry is less than the speed of sound. This assumption may be violated locally at the instant of impact of the leading edge with the water surface due to the large accelerations.

(*d*) The effects of surface tension are ignored – it primarily affects the formation of spray in the splash region.

(*e*) The hydrofoil is assumed to be rigid. This neglects any possible interaction between the fluid and the hydrofoil due to vibration. (The propeller blade vibrates as a consequence of the cyclic loading and unloading as it enters and exits the water surface.) Experimental observations for surface-piercing propellers (Olofsson 1996) indicate that the effects of vibration are not important during the entry phase of the blade passage. A rigid-blade assumption is sufficient as the emphasis here is mainly on the entry phase.

2.1. *Unique aspects of the flow*

(a) *Inception of ventilation*: The inception of ventilation is too complicated a process to be modelled accurately within the framework of potential theory. The linear and

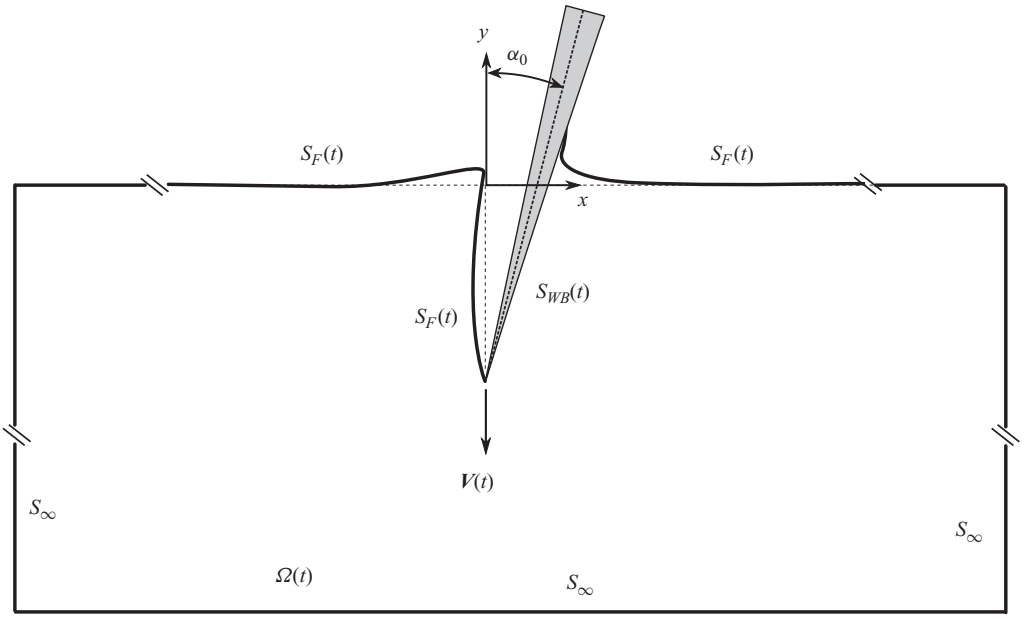

FIGURE 1. Ventilating entry of a hydrofoil section: fluid domain and corresponding boundaries.

nonlinear theoretical models described in § 1 assume the hydrofoil to be ventilating from the very beginning, with ventilation starting at the leading edge.

(b) *Detachment locations*: The ventilated surface is nothing but a cavity that vents into the atmosphere and is maintained at atmospheric pressure. An important aspect of cavity flows is the problem of specifying the detachment location – the point at which the cavity separates from the body surface (Birkhoff & Zarantonello 1957; Gilbarg 1960). Fixed detachment is appropriate for cases where the point of detachment of the cavity is known *a priori*, for example, bodies with sharp leading edges. For smooth blade sections, say with round leading edges, the cavity detachment location is not known beforehand and has to be determined as a part of the solution. Since typical surface-piercing propeller sections have sharp leading edges, the ventilated surface is assumed to start right at the leading edge.

3. Mathematical formulation

Consider a rigid, wedge-shaped two-dimensional hydrofoil entering initially calm water with a constant velocity $\boldsymbol{V}$ and an angle of attack α_0, as shown in figure 1. A fixed (non-rotating) Cartesian coordinate system is chosen to represent the flow with its origin at the undisturbed water level. The flow is represented in terms of a velocity potential $\phi(\boldsymbol{x}, t)$, with the local fluid velocity given by $\boldsymbol{q}(\boldsymbol{x}, t) = \nabla\phi = (\phi_x, \phi_y) = (u, v)$. Here, $\boldsymbol{x} = (x, y)$ represents the spatial location with respect to the fixed coordinate system, with x being the horizontal measure and y the vertical measure positive upwards. The fluid domain and the corresponding boundary surfaces are shown in figure 1. $S_{WB}(t)$ represents the 'wetted' part of the hydrofoil surface, $S_F(t)$ is the free

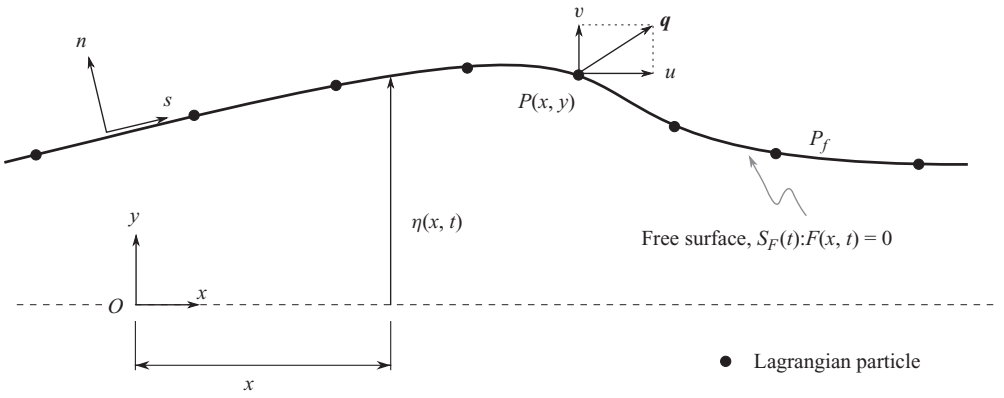

FIGURE 2. Free-surface schematic showing the application of fully nonlinear free-surface boundary conditions.

surface that also includes a part of the ventilated surface on the suction side of the hydrofoil and S_∞ is the far-field boundary.

3.1. *Boundary integral equation*

A boundary integral equation (BIE) is solved at each time step of a higher order time-stepping scheme in order to obtain the velocity potential. Once the solution is obtained for a particular time, the time-dependent boundary conditions are updated and the solution scheme progresses onto the next one.

The boundary-value problem for the velocity potential is converted into a BIE by introducing a two-dimensional Green's function $G(\boldsymbol{p}, \boldsymbol{q}) = (-1/2\pi) \ln r_{\boldsymbol{pq}}$ (satisfying the Laplace equation), where $r_{\boldsymbol{pq}} = |\boldsymbol{p} - \boldsymbol{q}|$, $\boldsymbol{p} \equiv \boldsymbol{p}(\boldsymbol{x})$ is the field point and $\boldsymbol{q} \equiv \boldsymbol{q}(\boldsymbol{x})$ is the source point. The BIE obtained by applying Green's third identity to $\phi(\boldsymbol{x}, t)$ and $G(\boldsymbol{p}, \boldsymbol{q})$ is

$$\alpha(\boldsymbol{p})\phi(\boldsymbol{p}) + \int_\Gamma \phi(\boldsymbol{q}) G_n(\boldsymbol{p}, \boldsymbol{q}) \, \mathrm{d}\Gamma_{\boldsymbol{q}} = \int_\Gamma G(\boldsymbol{p}, \boldsymbol{q}) \phi_n(\boldsymbol{q}) \, \mathrm{d}\Gamma_{\boldsymbol{q}}, \tag{3.1}$$

where $2\pi\alpha(\boldsymbol{p})$ is the internal angle formed at the boundaries, $G_n(\boldsymbol{p}, \boldsymbol{q}) = \nabla G(\boldsymbol{p}, \boldsymbol{q}) \cdot \boldsymbol{n}_{\boldsymbol{q}}$ and $\phi_n(\boldsymbol{p}, \boldsymbol{q}) = \nabla \phi(\boldsymbol{p}, \boldsymbol{q}) \cdot \boldsymbol{n}_{\boldsymbol{q}}$, with $\boldsymbol{n}_{\boldsymbol{q}}$ being the normal vector at $\boldsymbol{q}$, positive out of the fluid. Note that Γ represents all the boundaries of the fluid domain.

3.2. *Kinematic boundary condition on $S_F(t)$*

The kinematic boundary condition (KBC) is obtained by assuming $S_F(t)$ to be a bounding surface, i.e. no material passes across the free surface (Dussan V. 1976). Based on the schematic shown in figure 2, if we represent the free surface as $F(\boldsymbol{x}, t) = y - \eta(x, t) = 0$, the KBC on the free surface is given by (Wehausen & Laitone 1960; Dussan V. 1976)

$$\frac{\mathrm{D}}{\mathrm{D}t} F(\boldsymbol{x}, t) = 0, \tag{3.2}$$

where $\mathrm{D}/\mathrm{D}t = (\partial/\partial t) + \nabla\phi \cdot \nabla$ is the material derivative. The parameter $\boldsymbol{q} = \nabla\phi = (\phi_x, \phi_y)$ is the fluid velocity on the free surface and $y = \eta(x, t)$ is the free-surface elevation.

From a Lagrangian particle representation of the free surface, for a particle $P(x, y)$ on the free surface, the KBC is given by (Dussan V. 1976; Longuet-Higgins & Cokelet 1976; Panton 1984)

$$\frac{\mathrm{D}\boldsymbol{x}}{\mathrm{D}t} = \nabla\phi \quad \text{or} \quad \left\{ \begin{array}{l} \dfrac{\mathrm{D}x}{\mathrm{D}t} = u = \phi_x \\ \dfrac{\mathrm{D}y}{\mathrm{D}t} = v = \phi_y \end{array} \right\}, \quad \boldsymbol{x} \in S_F(t). \tag{3.3}$$

The dynamic boundary condition (DBC) is obtained from Bernoulli's equation and by assuming the pressure to be continuous across the free surface. It is assumed that the wavelength of the free-surface elevation is long enough to neglect the effects of surface tension. Thus, the pressure underneath the free surface must equal the atmospheric pressure above, yielding the most general form of the free-surface DBC:

$$\frac{\partial\phi}{\partial t} + \tfrac{1}{2}|\nabla\phi|^2 + g\eta + \frac{P_f}{\rho} = 0, \quad \boldsymbol{x} \in S_F(t), \tag{3.4}$$

where g is the acceleration due to gravity. The common form of the DBC is obtained by expressing the pressure as gage pressure, in which case the pressure on the free surface $P_f = P - P_{atm} = 0$. For a Lagrangian particle $P(x, y)$, the DBC can be rewritten as

$$\frac{\mathrm{D}\phi}{\mathrm{D}t} = \tfrac{1}{2}|\nabla\phi|^2 - g\eta, \quad \boldsymbol{x} \in S_F(t). \tag{3.5}$$

3.3. *Boundary condition on hydrofoil $S_{WB}(t)$*

On the 'wetted' part of the hydrofoil surface $S_{WB}(t)$,

$$\nabla\phi \cdot \boldsymbol{n} = \boldsymbol{V}(t) \cdot \boldsymbol{n}, \quad \boldsymbol{x} \in S_{WB}(t), \tag{3.6}$$

where $\boldsymbol{V}(t)$ is the prescribed velocity of the hydrofoil. For the surface entry of a hydrofoil moving vertically downwards with a constant velocity V_w, the velocity $\boldsymbol{V}(t) = (0, -V_w)$.

3.4. *Boundary condition on far-field boundary S_∞*

The far-field boundary S_∞ is assumed to be a no-flux surface with

$$\nabla\phi \cdot \boldsymbol{n} = 0, \quad \boldsymbol{x} \in S_\infty, \tag{3.7}$$

and special attention is paid to placing the boundary far away from the body to avoid reflection of the waves generated by its motion. In terms of physical dimensions, it was found sufficient to have the boundary about $10c$ away from the hydrofoil, where c is the chord length of the hydrofoil under consideration.

3.5. *Initial conditions*

The initial conditions for this problem depend on the angle of attack α_0 and the existence of a ventilated surface on the suction side of the hydrofoil.

(*a*) For a fully wetted flow, a tiny fraction of the wedge is assumed to be initially immersed. The solution is started impulsively and allowed to progress until the hydrofoil is completely immersed.

(*b*) The treatment of the fully ventilating case requires special attention. For a hydrofoil with a sharp leading edge, ventilation is triggered right at the leading

edge. However, during the process of the development of the method it was found extremely difficult to numerically 'trigger' ventilation at the leading edge. According to Wang (1977) the flow field surrounding a ventilating hydrofoil is identical to that of a supercavitating flat plate (in an unbounded fluid domain) with zero cavitation number. This aspect of the flow forms the basis for getting the initial conditions for the ventilating flow. The proposed model consists of the following steps: (i) Assume an initial shape of the ventilated surface – the initial shape is derived from the analytical expressions for the supercavity produced by a flat plate in an infinite flow domain. These expressions are obtained from the free-streamline theory of Wu (1955). The initial surface length is assumed to be a fraction of the chord length of the hydrofoil. (ii) Instead of being treated as a free surface, the initial shape of the ventilated surface is assumed to be rigid or wetted. With this assumption, the free-surface problem is solved as an asymmetric water entry. (iii) After the hydrofoil has travelled a certain distance, part of the initial surface assumed to be wetted is appended to the adjoining free surface. (iv) The actual solution of the ventilating problem starts from this point onwards. The intersection of the initial ventilated surface (modelled as wetted) and the free surface is treated as a fixed separation point. The solution is allowed to progress with the free surface on the suction side continuously detaching from the intersection point.

3.6. *Treatment at a fixed separation point*

At the fixed separation point, the normal velocity of the free surface is assumed to be the same as that of the hydrofoil. This assumption ensures continuity of slope between the wetted body and the ventilated surface. This is consistent with the analytical solution for the local flow presented in Faltinsen (2005) and Zhao, Faltinsen & Aarsnes (1996). The potential is inherently continuous by virtue of the use of linear isoparametric elements. The BIE is not solved at the separation point as both the primary variable (ϕ) and the secondary variable (ϕ_n) are known.

4. Numerical formulation

A brief summary of the important numerical aspects of the scheme is presented here. Details of the numerical scheme can be found in Vinayan (2009).

(*a*) A mixed Eulerian–Lagrangian (MEL) scheme of Longuet-Higgins & Cokelet (1976) is used to solve the initial boundary-value problems presented in the previous section. The MEL scheme comprises primarily two steps: (i) solve a well-defined boundary-value problem based on a given set of boundary conditions using the BEM and (ii) update the free-surface geometry and potential on the free surface by time integration of the fully nonlinear kinematic and dynamic free-surface boundary conditions. These two steps are repeated at each time step of a fourth-order Runge–Kutta time-marching scheme. The proper implementation and solution of the two MEL steps dominate the numerical implementation of the free-surface problem.

(*b*) Linear iso-parametric elements form the basis for the numerical solution of the BIE. A 'double-node' approach is used at the corners of the domain. However, the BIE is not solved at a double node if it happens to be a separation point.

(*c*) The treatment of the jet that forms along the wetted side of the hydrofoil is similar to that presented in Kihara (2006) and Sun & Faltinsen (2007). The jet is allowed to grow until a threshold angle is reached between the jet and the adjoining

body surface. Once this limiting angle is reached a new panel is created at an angle greater than the threshold value. The intersection of the new panel with body surface becomes the new body–free-surface intersection point. The angle is continuously monitored during the solution and the 'cut-off' process is implemented every time it is less than the threshold value. The value of the threshold angle is chosen to be $\pi/15$, a value chosen to correspond to the analytical solutions presented in Dobrovol'skaya (1969).

(*d*) A re-panelling scheme is implemented to maintain sufficient and uniform resolution in the area of the jet. Even though linear elements are used to model the free surface, re-panelling is performed using a cubic spline scheme with the arc length of the surface as a parameter instead of the Euclidean distance. The arc length is calculated by first fitting a cubic spline with the node index as a parameter. With the cubic spline coefficients, the arc length is calculated numerically using a 12-point Gauss–Legendre quadrature. This approach was suggested in Longuet-Higgins & Cokelet (1976) to maintain the accuracy of the re-panelling scheme.

(*e*) A third-order five-point least-squares model is implemented to smooth instabilities that arise during the simulation. The smoothing scheme was found to be necessary to smooth out oscillations resulting from the impulsive start of the wetted problem and applied only at an interval of 10 time steps. Moreover, the smoothing process is applied only close to the intersection between the free surface and the hydrofoil.

(*f*) The pressure on the body surface is obtained from Bernoulli's equation

$$\frac{P}{\rho} = -\frac{\partial \phi}{\partial t} - \tfrac{1}{2}|\nabla \phi|^2 - gy. \tag{4.1}$$

The critical part of this expression for the pressure is the evaluation of the time derivative $\partial\phi/\partial t$. In particular, it is important to note that the body surface changes with time and also due to re-gridding. Taking these factors into consideration, we have

$$\frac{\delta \phi}{\delta t} = \frac{\partial \phi}{\partial t} + \boldsymbol{V}_g \cdot \nabla \phi, \tag{4.2}$$

where $\delta\phi/\delta t$ is used to represent the change in ϕ where one follows a point that moves with a velocity $\boldsymbol{V}_g$, which is different from the fluid velocity. This can be seen as a generalization of the material derivative and is with respect to a coordinate system moving with a constant velocity. To calculate the pressure on the body, $\boldsymbol{V}_g$ is set to the local grid velocity of the body surface.

From (4.1) and (4.2), we have

$$\frac{P}{\rho} = -\frac{\delta \phi}{\delta t} + \boldsymbol{V}_g \cdot \nabla \phi - \tfrac{1}{2}|\nabla \phi|^2 - gy. \tag{4.3}$$

The corresponding pressure coefficient is defined as

$$C_p = \frac{2(P - P_{atm})}{\rho V_w^2}. \tag{4.4}$$

5. Validation of the numerical algorithm

The numerical features of the scheme presented in the previous section are thoroughly validated through a comparison with analytical self-similar solutions. The first set of validations shown in figures 3 and 4, respectively, compare the free-surface

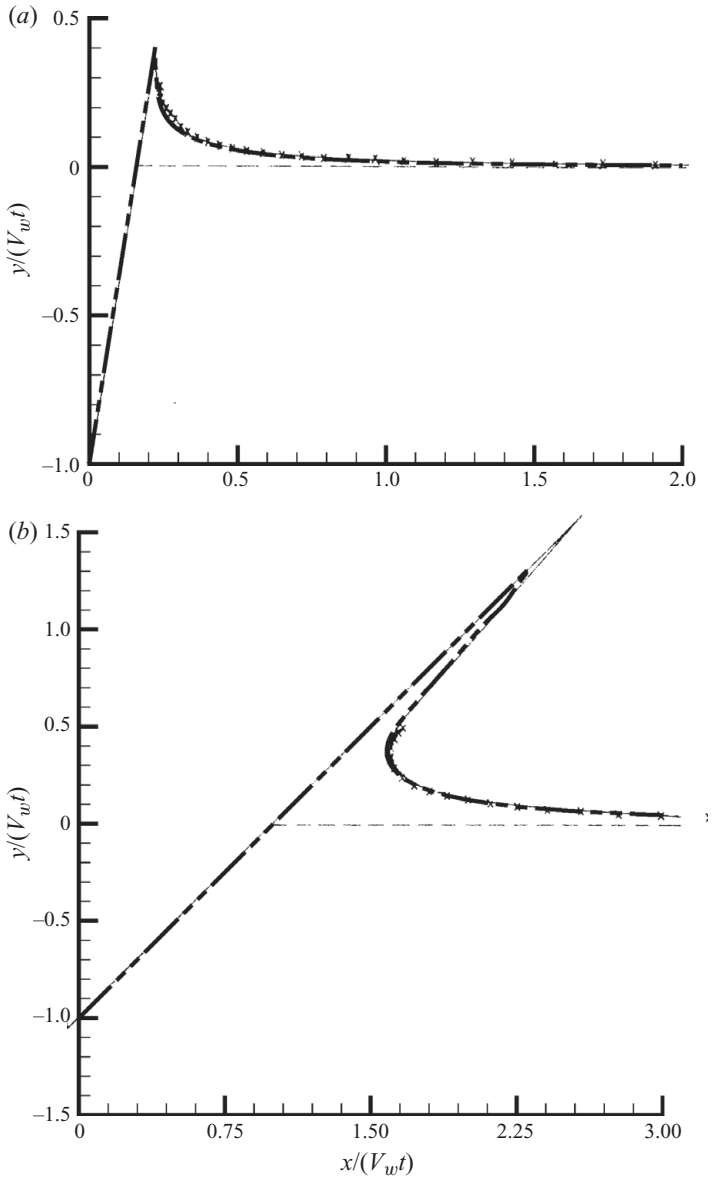

FIGURE 3. Predicted free-surface elevation during water entry of a wedge with constant vertical velocity (V_w) (symmetric entry with no ventilation). Comparison between ——, similarity solution (Zhao & Faltinsen 1993); × × × × ×, BEM (Zhao & Faltinsen 1993); — · · — · · —, current BEM. (*a*) Deadrise angle = 81°. (*b*) Deadrise angle = 45°.

elevations and pressure distributions predicted by the current scheme along with the boundary-element solution of Zhao & Faltinsen (1993) and self-similar solution of Dobrovol'skaya (1969) and Zhao & Faltinsen (1993). The results shown are for the symmetric water entry of a wedge at a constant vertical velocity (V_w). It can be observed from figure 3 that the current scheme is able to retain the jet over a longer part of the wedge and agrees well with the self-similar solution. A similar observation can be made in the case of the pressure distributions, as seen in figure 4.

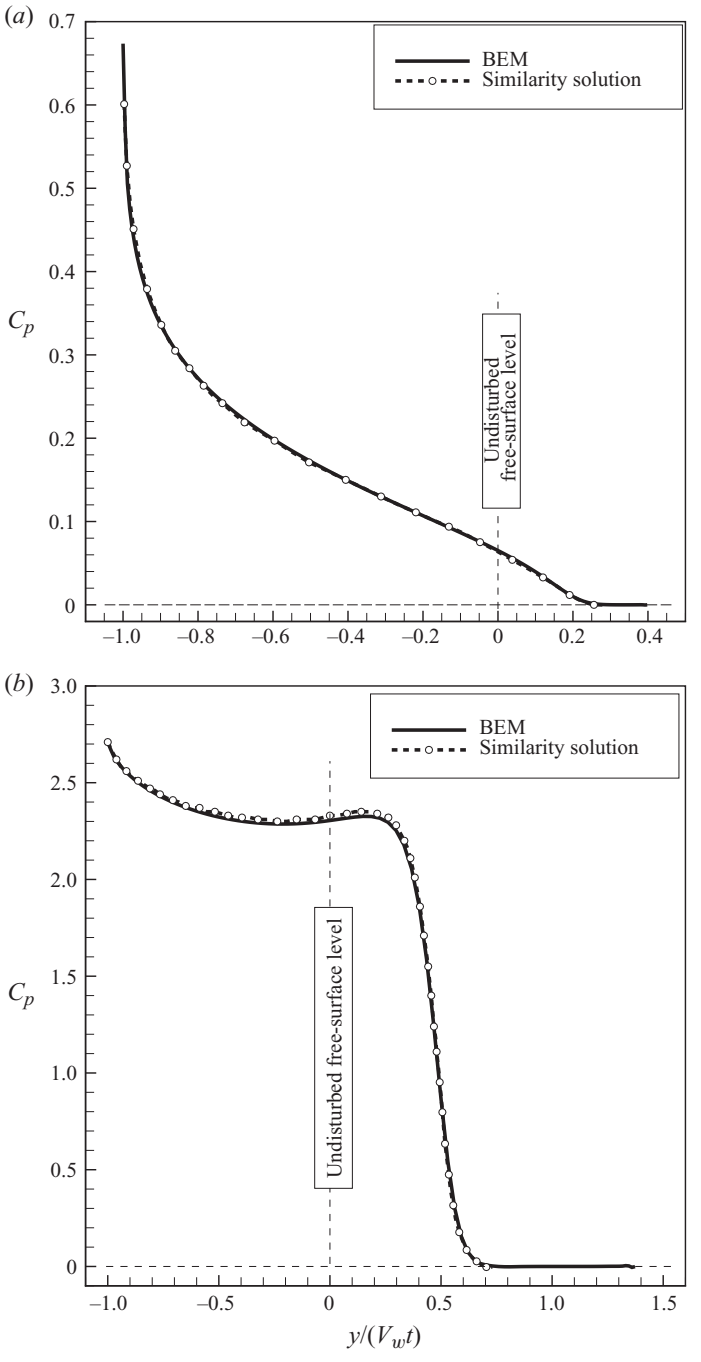

FIGURE 4. Predicted pressure distribution during water entry of a wedge with constant vertical velocity (V_w) (symmetric entry with no ventilation). Comparison between similarity solution of Dobrovol'skaya (1969) and Zhao & Faltinsen (1993) and current BEM. (*a*) Deadrise angle = 81°. (*b*) Deadrise angle = 45°.

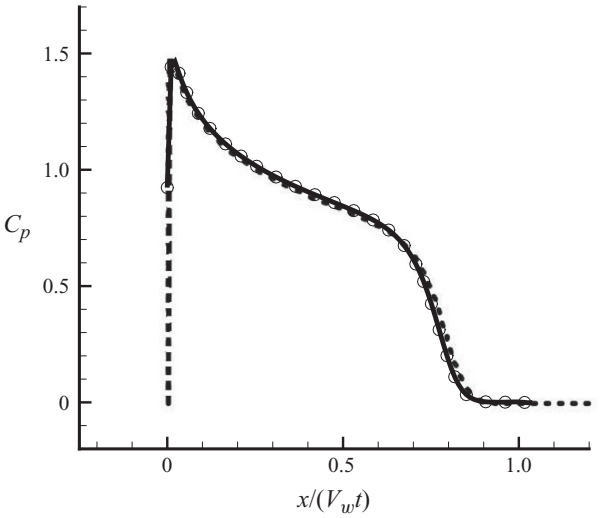

FIGURE 5. Predicted pressure distribution during ventilating water entry of a flat plate at an angle of attack of 30°. Comparison between - - - -, analytical similarity solution of Faltinsen & Semenov (2008) and –○–, current BEM.

The second validation is for the ventilating entry of a flat plate at an angle of attack of 30°. A comparison of the predicted pressures, between the current scheme and the analytical self-similar solution of Faltinsen & Semenov (2008), is shown in figure 5. Note that the pressures shown are for the wetted part (pressure side) of the plate with the suction side completely ventilated. The overall comparison is good and this further validates the current scheme.

6. Results

Cox (1971) conducted a series of experiments with a symmetric wedge of dimensions 12.7 mm (0.5 in.) × 152.4 mm (6 in.) with a chord length of 152.4 mm (6 in.). In the experiments, the wedge was dropped from different heights (equivalent to changing the velocity of entry V_w) and at different angles of attack, α_0. For each instance, the ventilated-surface shape was photographed after the wedge had approximately travelled its length through the water surface. These photographs provide an excellent source of validation for the BEM model. As a representative case, a velocity of entry of 2.45 m s^{-1} (corresponding to a drop of 304.8 mm) is chosen for validation. All the subsequent BEM results correspond to this geometry and velocity.

In the subsequent calculations N_{WB}, $N_{F,s}$, $N_{F,p}$ and N_∞ represent the total number of panels on the wetted part of hydrofoil, the free surface on the pressure side, the free surface on the suction side and the far-field boundary, respectively.

6.1. *Convergence characteristics and effect of the initial condition*

It was mentioned in the numerical formulation that an initial guess for the ventilated-surface shape is obtained from the corresponding solution of a supercavitating flat plate. The length initially guessed is expressed as a percentage of the total chord c of the hydrofoil and is represented by the parameter δ_{iv}. Figure 6 shows the effect of the parameter δ_{iv} on the final ventilated-surface shape. (The simulation is stopped once the free surface on the wetted side reaches the base of the wedge.) In terms of a chord length $c = 152.4$ mm, the minimum δ_{iv} of 2 %c would be about 3 mm, while

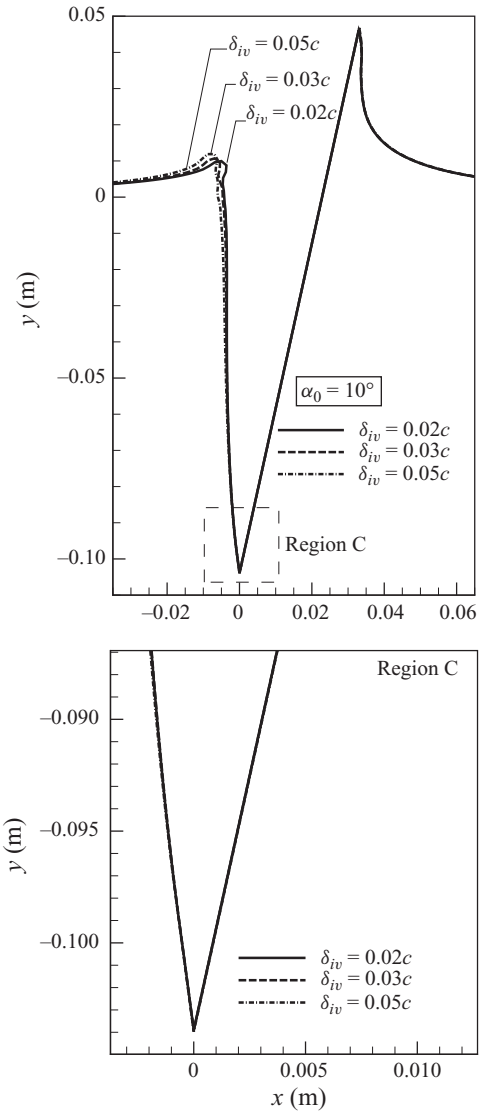

FIGURE 6. Ventilating entry of a surface-piercing wedge: effect of the parameter δ_{iv} on the ventilated-surface shape. Region C: magnified view of the ventilated-surface shape close to the leading edge of the hydrofoil. (no discernible difference is seen in the surface shapes for different δ_{iv})

the maximum would be about 7 mm. On the whole, the parameter δ_{iv} does not affect the final shape of the ventilated surface and the free-surface elevation on the wetted side. Differences are observed in the region where the vertical part of the ventilated surface meets the horizontal free surface. The similarity solutions of Chekin (1989) and Faltinsen & Semenov (2008) predict a cusp at the point where the two convex free surfaces meet. This aspect of the flow is not considered in the numerical scheme and leads to the observed differences. Figure 7 shows the effect of δ_{iv} on the wetted-side pressure and no discernible differences are observed. (All the subsequent calculations are with $\delta_{iv} = 2\,\%c$.)

The convergence of the ventilated-surface shape with respect to a change in the number of panels on the surface is shown in figure 8, where $N_{F,s}$ represents the

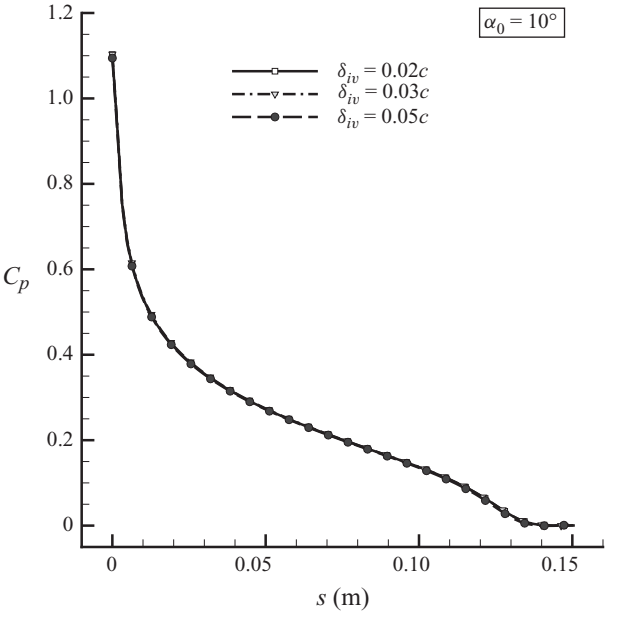

FIGURE 7. Ventilating entry of a surface-piercing wedge: effect of the parameter δ_{iv} on the pressure predicted on the wetted part of the hydrofoil. C_p is the pressure coefficient and s is the arc length along the wedge surface.

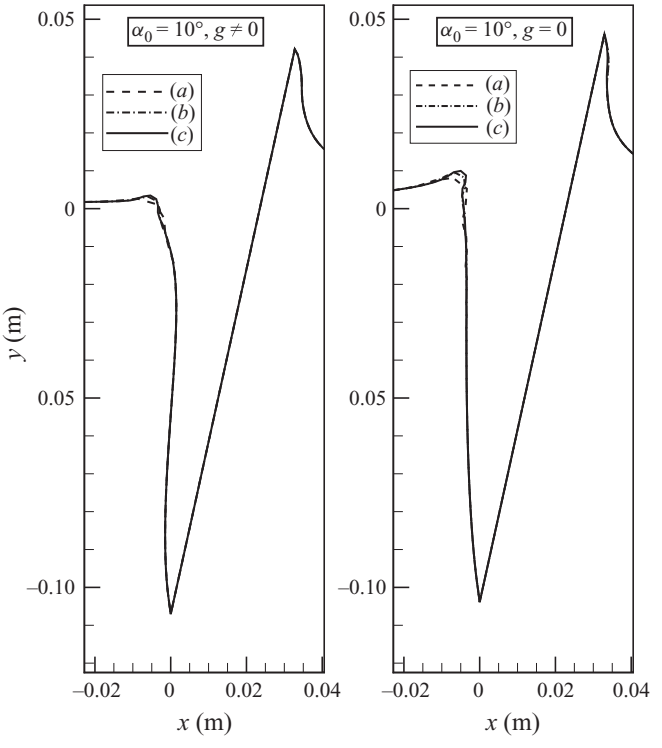

FIGURE 8. Ventilating entry of a surface-piercing wedge: convergence characteristics of the ventilated-surface shape with respect to the number of panels on the surface. (*a*) $N_{F,s} = 125$; (*b*) $N_{F,s} = 215$; (*c*) $N_{F,s} = 300$; $g \neq 0$ corresponds to $F_{nc} = 2.0$.

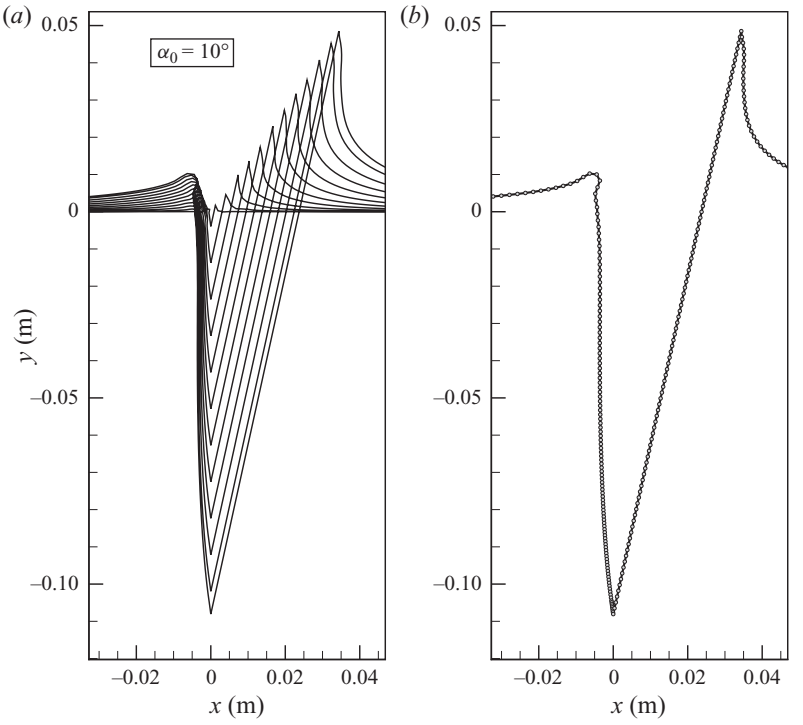

FIGURE 9. Ventilating entry of a surface-piercing wedge: free-surface and ventilated-surface shapes predicted by the BEM scheme in the absence of gravity ($g = 0$) (*a*) at different stages of entry and (*b*) at time $t = 0.0419$ s. Parameters of the simulation: $\Delta t = 10^{-4}$ s, $N_{WB} = 100$, $N_{F,s} = 300$, $N_{F,p} = 125$, $N_{\infty} = 40$, Δt is the time step.

number of panels on the entire free surface, including the ventilated surface, on the suction side of the hydrofoil.

6.2. *Effect of gravity*

Figures 9 and 10, respectively, show the ventilated surfaces for different levels of submergence, without ($g = 0$) and with ($g \neq 0$) the effects of gravity. Figures 11 and 12 show the corresponding pressure distributions on the wetted part of the wedge. Defining a Froude number in terms of the chord length c as $F_{nc} = V_w/\sqrt{gc}$, $g = 0$ would correspond to $F_{nc} = \infty$ and $g \neq 0$ to $F_{nc} = 2$. (Note that in the figures, only the wetted boundary of the hydrofoil is shown. Although the thickness form is not shown, the ventilated surface does not intersect the suction side of the hydrofoil.) The effect of gravity becomes apparent when the free-surface elevations are expressed in terms of the similarity variables, as shown in figure 13. In the absence of gravity all the free-surface profiles, starting with the first instance when similarity is observed to the end of the simulation, are seen to overlap. The scheme is able to preserve the self-similarity of the flow. The lack of self-similarity, as expected, can be observed in figure 13 when the effect of gravity is included.

6.3. *Comparison with experiments*

In figure 14, a comparison between the predicted ventilated surface and that observed from the experiments of Cox (1971) is shown for an angle of attack of 10°. The free-surface elevation and the ventilated surface are compared for the same level of submergence. There appear to be two lines representing the ventilated surface in

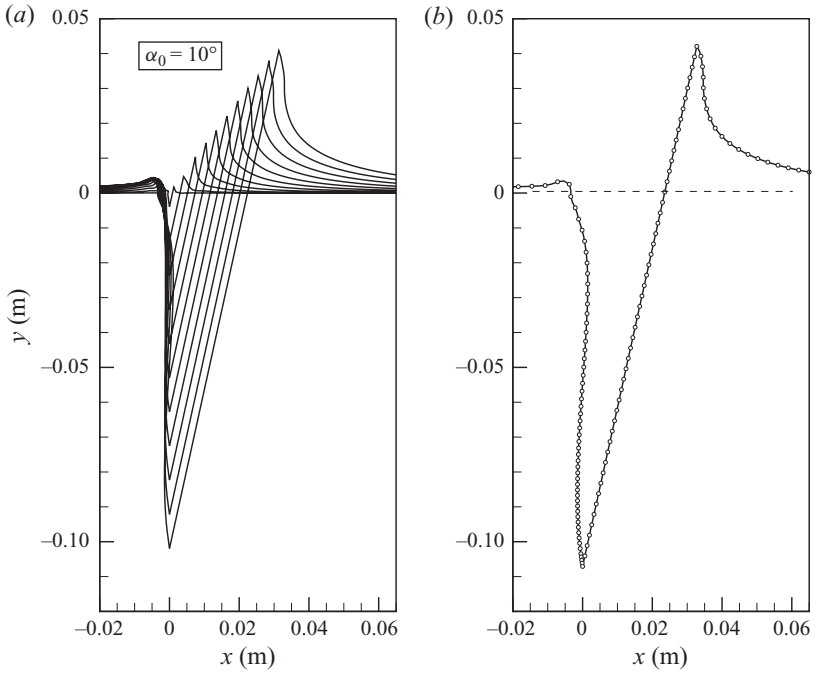

FIGURE 10. Ventilating entry of a surface-piercing wedge: free-surface and ventilated-surface shapes predicted by the BEM scheme in the presence of gravity ($g \neq 0$) (*a*) at different stages of entry and (*b*) at time $t = 0.0432$ s. Parameters of the simulation: $\Delta t = 10^{-4}$ s, $N_{WB} = 100$, $N_{F,s} = 300$, $N_{F,p} = 125$, $N_{\infty} = 40$; $g \neq 0$ corresponds to $F_{nc} = 2.0$.

the photograph. Cox (1971) attributes this to the presence of glass walls that form the boundaries of the experimental tank set-up. The outline farthest away from the wedge that is generally convex to the fluid is presumably the location of the boundary-layer attachment on the glass. This layer is formed due to the large retarding forces experienced by the fluid particles close to the glass surface. Cox (1971) mentions that the inner line represents the actual surface over most of the chord. Based on these observations, it can be seen that the overall agreement between the predicted and the experimentally ventilated surfaces is good.

A similar comparison between the experimental and predicted results is shown in figure 15 for smaller angles of attack of 0°, 2° and 4° respectively. In each of these cases, the experimental photographs indicate that there is no ventilation on the suction side of the wedge. In line with these observations the numerical predictions are performed with both sides of the wedge wetted, i.e. the pressure and suction sides of the wedge are assumed to be fully wetted (unlike the ventilating case where the suction side is not wetted). The fully wetted formulation presented along with the validation studies is used here with the wedge entering the water surface at the specified angle of attack. For all the three angles of attack considered here, the comparison between the predicted and experimental results is satisfactory.

6.4. *Comparison with linear free-surface model*

A comparison of the pressure distribution along the wetted face between the method of Savineau & Kinnas (1995) (linear) and the current nonlinear method is shown in figure 17. The linear method is clearly deficient in terms of capturing the excess pressure due to the nonlinear free-surface effects. The excess pressure corresponds to

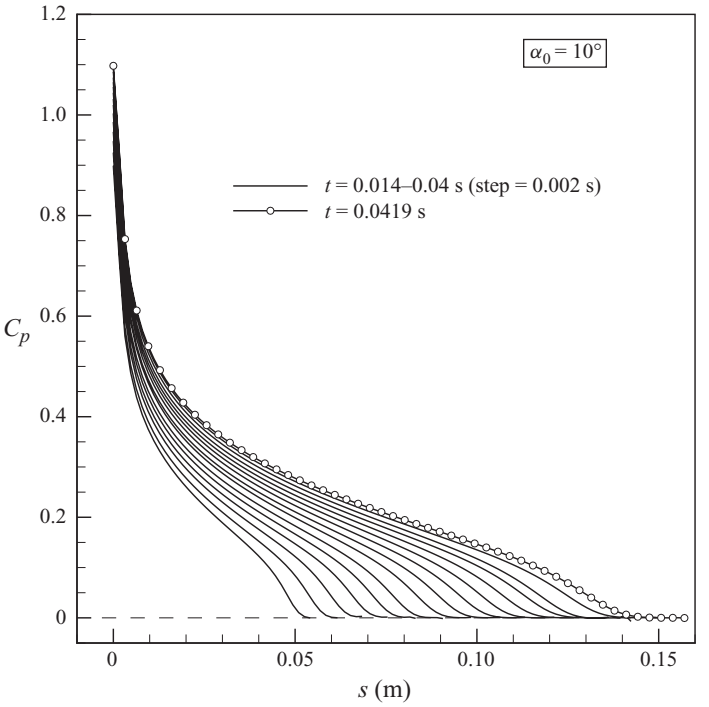

FIGURE 11. Ventilating entry of a surface-piercing wedge: pressure along the wetted part of the hydrofoil at different stages of entry in the absence of gravity ($g = 0$). Parameters of the simulation: $\Delta t = 10^{-4}$ s, $N_{WB} = 100$, $N_{F,s} = 300$, $N_{F,p} = 125$ and $N_\infty = 40$. C_p is the pressure coefficient.

the region $y > 0$, where $y = 0$ corresponds to the undisturbed free-surface level. This difference was shown to exist even in the very early stages of entry in Vinayan & Kinnas (2008). Figures 16 and 17 highlight the shortcomings of the negative-image method and the importance of including the nonlinear free-surface effects.

6.5. *Effect of Froude number and angle of attack*

Shiba (1953) and Olofsson (1996) mention that in the fully ventilated regime, the effect of the Froude number is negligible when $F_n > 3$ (where $F_n = nD/\sqrt{gD}$ is the Froude number based on propeller diameter D and rotational speed n). This is because the ventilated cavities have asymptotically attained their final shapes and a subsequent increase in the Froude number makes no difference. A similar observation can be made from the two-dimensional solutions shown in figure 18. The ventilated surfaces are seen to converge rapidly towards the $F_{nc} = \infty$ ($g = 0$) shape. The effect of the Froude number on the suction side of the hydrofoil seems to be much stronger than that on the pressure side. This is so because on the pressure side the formation of spray is neglected. In the BEM-based numerical scheme, gaps are not allowed in the domain. This forces the free-surface–body intersection point to be on the body at all times and inhibits the formation of spray. Had the effect of spray been taken into account by allowing the free-surface jet formed on the pressure side to continuously separate from the body, one would have seen a stronger effect on the pressure side. It should be noted that the pressure over a large region of the jet is equal to zero (atmospheric) and thus its extent has negligible effect on the pressure distribution and the forces on the foil.

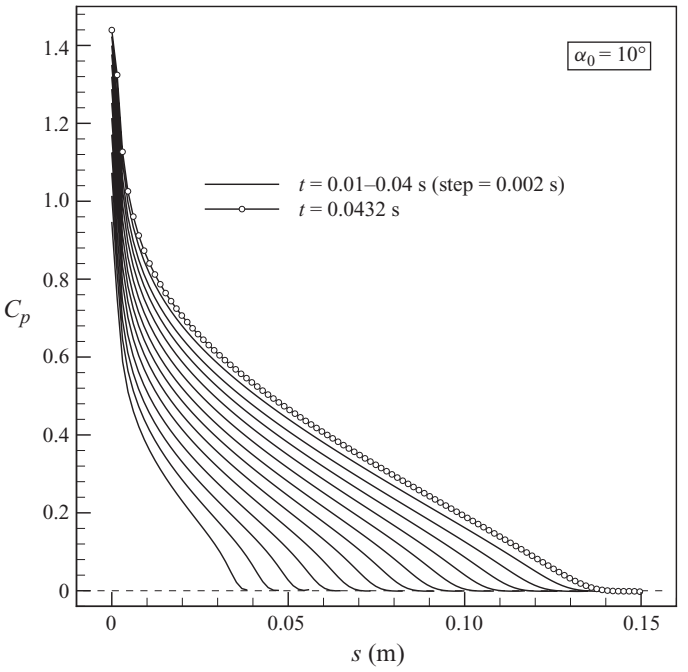

FIGURE 12. Ventilating entry of a surface-piercing wedge: pressure along the wetted part of the wedge at different stages of entry in the presence of gravity ($g \neq 0$). Parameters of the simulation: $\Delta t = 10^{-4}$ s, $N_{WB} = 100$, $N_{F,s} = 300$, $N_{F,p} = 125$, $N_\infty = 40$. C_p is the pressure coefficient; $g \neq 0$ corresponds to $F_{nc} = 2.0$.

The normal force coefficient C_n and its variation with respect to a change in the Froude number F_{nc} is shown in figure 19(a) for an angle of attack of $\alpha_0 = 10°$. Here C_n is defined as $f/((1/2)\rho V_w^2)$, where $f = \int P \mathrm{d}s$ is the normal force on the wetted part of the hydrofoil. As the Froude number increases, the contribution of the gravitational component of the pressure decreases, thus reducing its contribution to the normal force. The percentage error in the normal force coefficient ΔC_n measuring the effect of including gravity is shown in figure 19(b). There is a 50 % error at $F_{nc} = 2.0$, which decreases to approximately 8 % at $F_{nc} = 5.0$. Here $\Delta C_n = (C_n - C_{n\infty})/C_{n\infty} \times 100$, where $C_{n\infty}$ is the normal force corresponding to $F_{nc} = \infty$ ($g = 0$).

There is a direct correlation between $F_{nc} = V_w/\sqrt{gc}$, which can be interpreted as the Froude number corresponding to a propeller section of chord c and the Froude number $F_n = nD/\sqrt{gD}$. For a section of the propeller at radius r, the velocity of entry $V_w = r\omega$, where $\omega = 2\pi n$ is the angular velocity. Thus, we have $F_{nc} = F_n \pi \sqrt{2r^2/(cR)}$, where $R = D/2$ is the radius of the propeller. For a typical surface-piercing propeller with $c/D = 0.5$, tables 1 and 2, respectively, show the values of F_n for $r = 0.2R$ (at the hub) and $r = 0.7R$. Also shown in tables 1 and 2 are the percentage errors in the normal force coefficients compared to a no-gravity case (as shown in figure 19b). From the results at $r = 0.2R$, it can be inferred that even for $F_n > 3$, the effects of gravity cannot be neglected for sections close to the hub.

Figure 20 shows the effect of the angle of attack on the ventilated-surface shapes ($g \neq 0$ corresponds to $F_{nc} = 2$). The volume of the ventilated surface is seen to increase with a corresponding increase in the angle of attack. From the experimental results

F_{nc}	F_n	ΔC_n, % error
2	2.25	52.58
3	3.38	22.70
4	4.50	12.64
5	5.63	8.33
6	6.75	5.46

TABLE 1. Variation of F_n and the percentage error of the normal force coefficient with respect to F_{nc} at $r = 0.2R$.

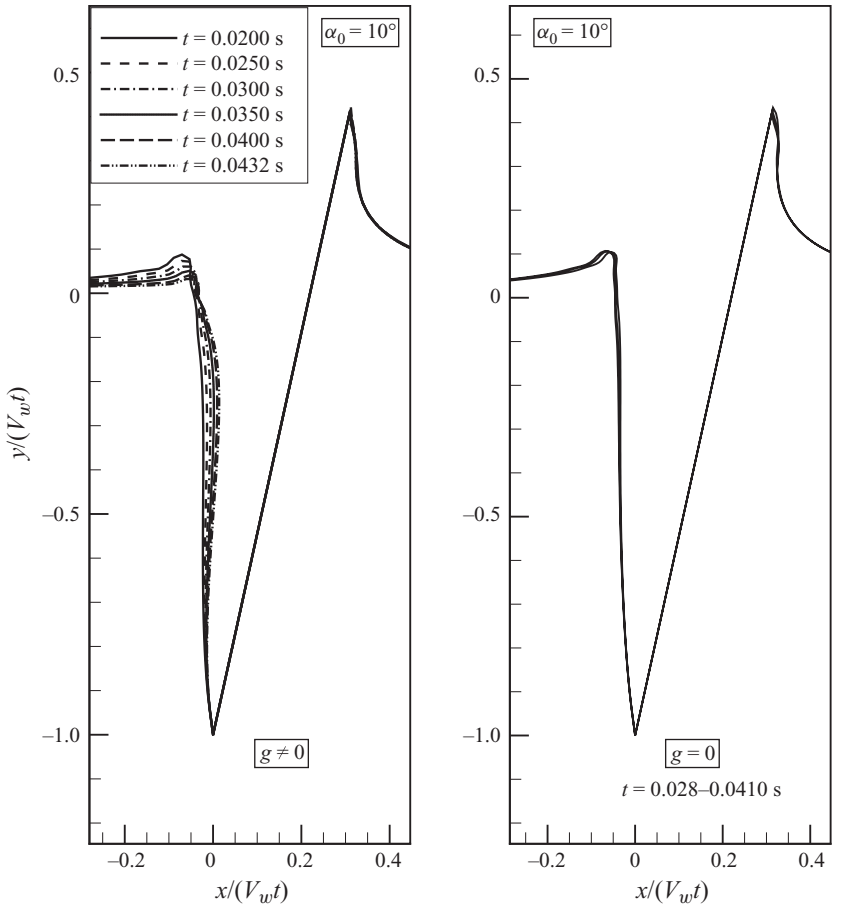

FIGURE 13. Ventilating entry of a surface-piercing wedge. Free-surface and ventilated-surface shape, with ($g \neq 0$) and without ($g = 0$) the presence of gravity, at different stages of entry expressed in terms of the similarity variables; $g \neq 0$ corresponds to $F_{nc} = 2.0$.

of Cox (1971), no ventilation is seen for angles less than 6°. For smaller angles of attack, the fully wetted mode can be used instead to calculate the pressure on the wedge. (See figure 15 for the free surface predicted when no ventilation is present.)

F_{nc}	F_n	ΔC_n, % error
2	0.64	52.58
3	0.96	22.70
4	1.29	12.64
5	1.61	8.33
6	1.93	5.46

TABLE 2. Variation of F_n and the percentage error of the normal force coefficient with respect to F_{nc} at $r = 0.7R$.

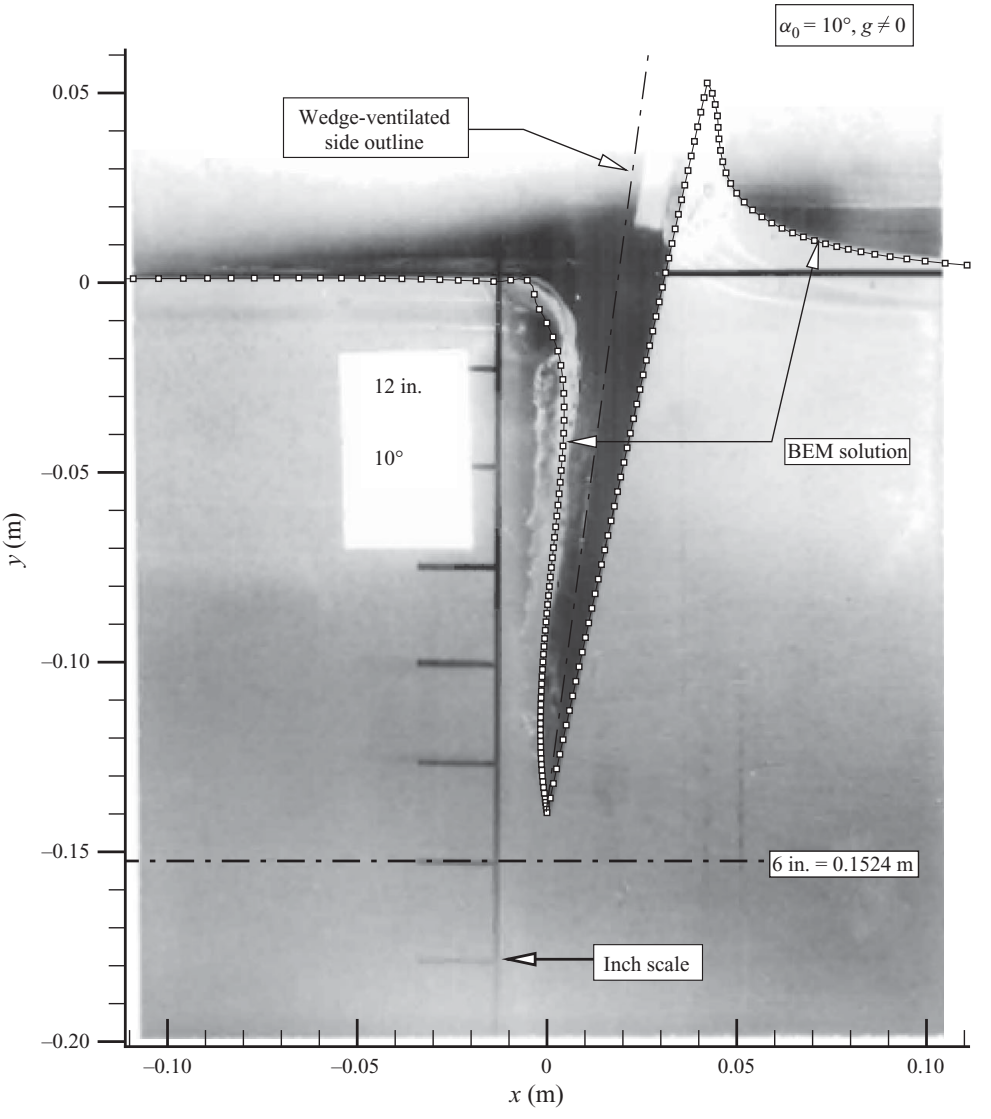

FIGURE 14. Ventilated-surface shape and free surface: comparison between experimental and numerical (BEM) results. $V_w = 2.45$ m s^{-1} corresponding to a 304.8 mm fall. (Photograph of experimental results from Cox (1971) used with permission.) $g \neq 0$ corresponds to $F_{nc} = 2.0$.

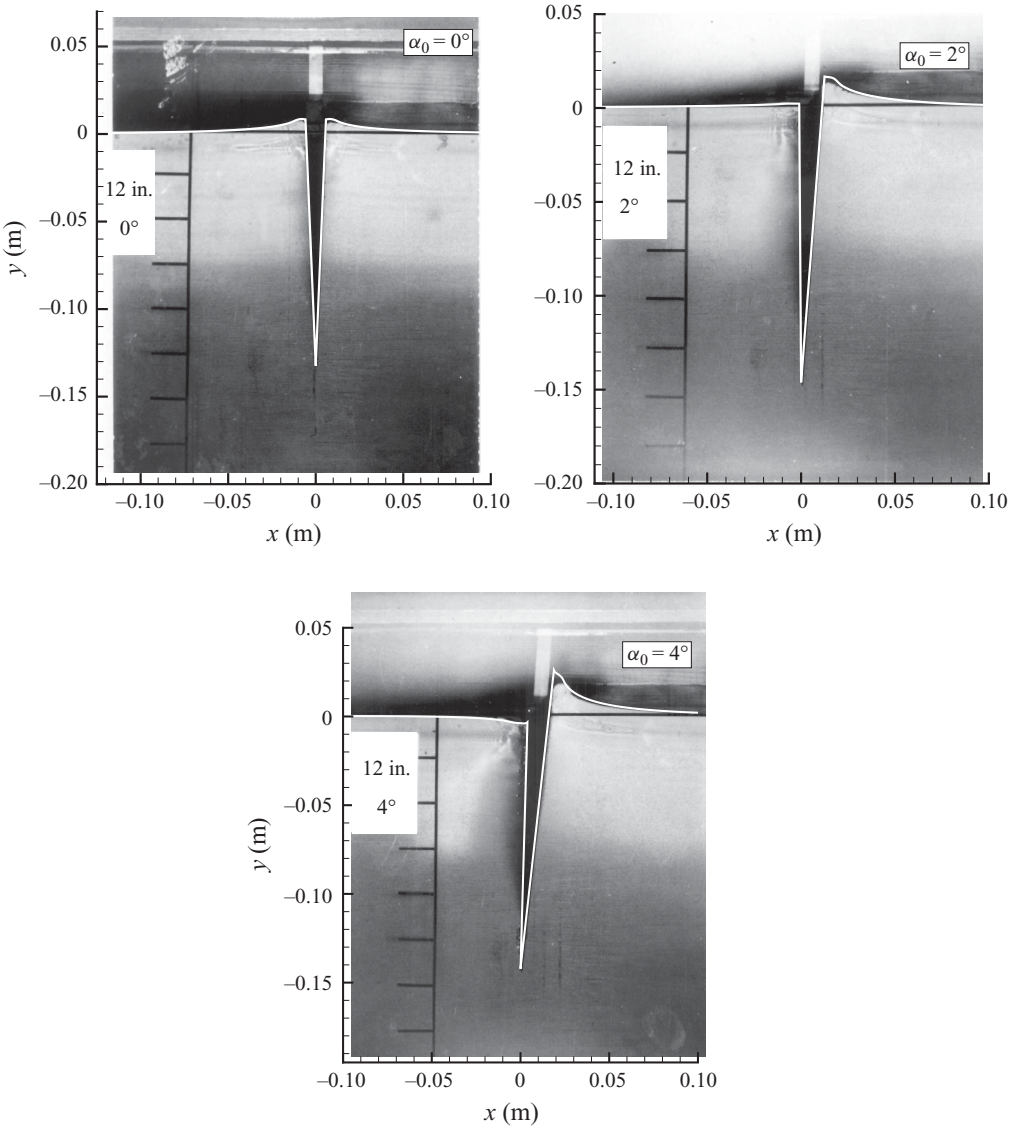

FIGURE 15. Ventilated-surface shape and free surface: comparison between experimental and numerical (BEM) results. $V_w = 2.45$ m s^{-1} corresponding to a 304.8 mm fall. (Photograph of experimental results from Cox (1971) used with permission.) Effects of gravity included.

7. Conclusions

A two-dimensional BEM-based numerical scheme has been developed to model the strongly nonlinear interaction between a ventilating surface-piercing hydrofoil and the free surface. The features of the current scheme that can be seen as an important contribution towards improving the performance prediction of surface-piercing propellers are the following:

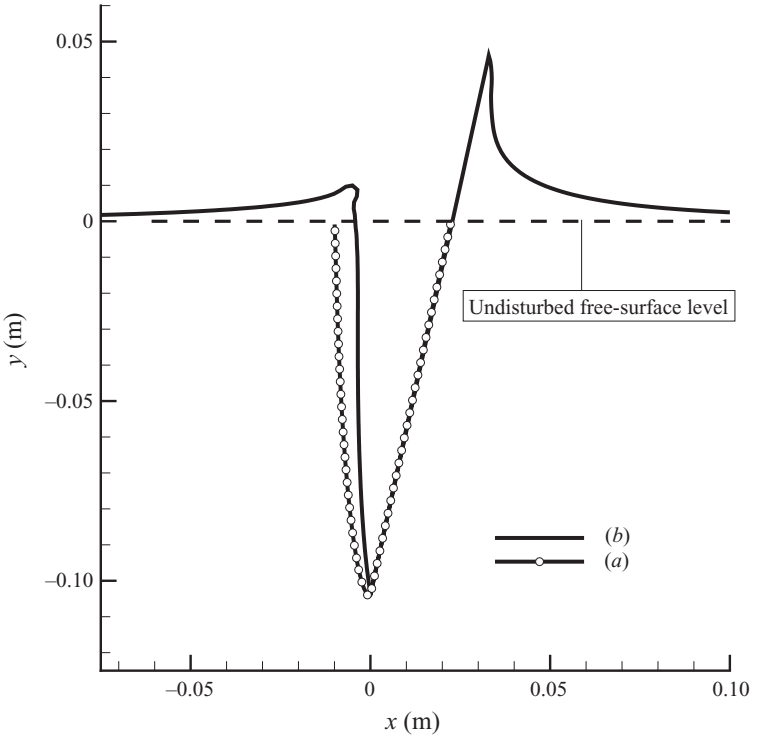

FIGURE 16. Ventilating entry of a surface-piercing wedge: comparison of ventilated-surface shapes between (*a*) linear method (Savineau & Kinnas 1995) and (*b*) current method. $V_w = 2.45$ m s^{-1} corresponding to a 304.8 mm fall. Angle of attack $\alpha_0 = 10°$.

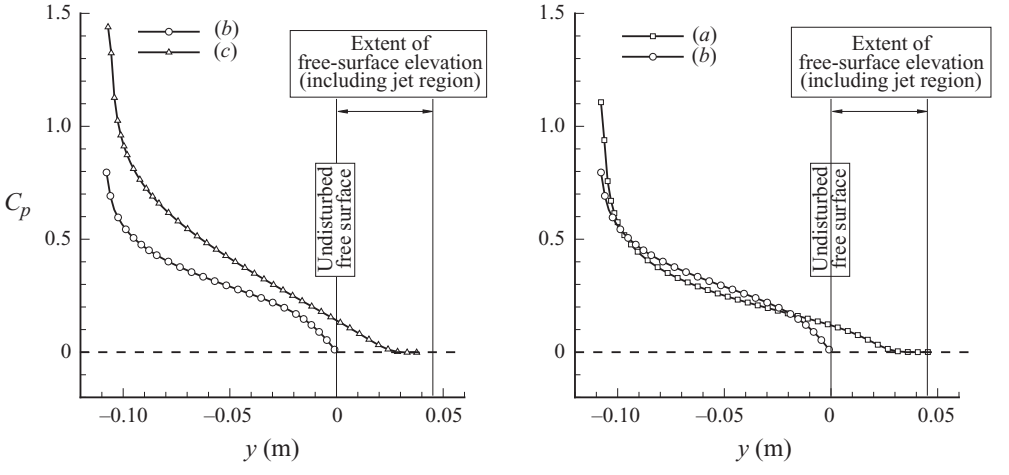

FIGURE 17. Ventilating entry of a surface-piercing wedge: comparison of pressure along the wetted part of the hydrofoil from linear method (Savineau & Kinnas 1995) and current method. (*a*) Current method ($g = 0$), (*b*) linear method (Savineau & Kinnas 1995) ($g = 0$), (*c*) current method ($g \neq 0$); $V_w = 2.45$ m s^{-1} corresponding to a 304.8 mm fall. Angle of attack $\alpha_0 = 10°$.

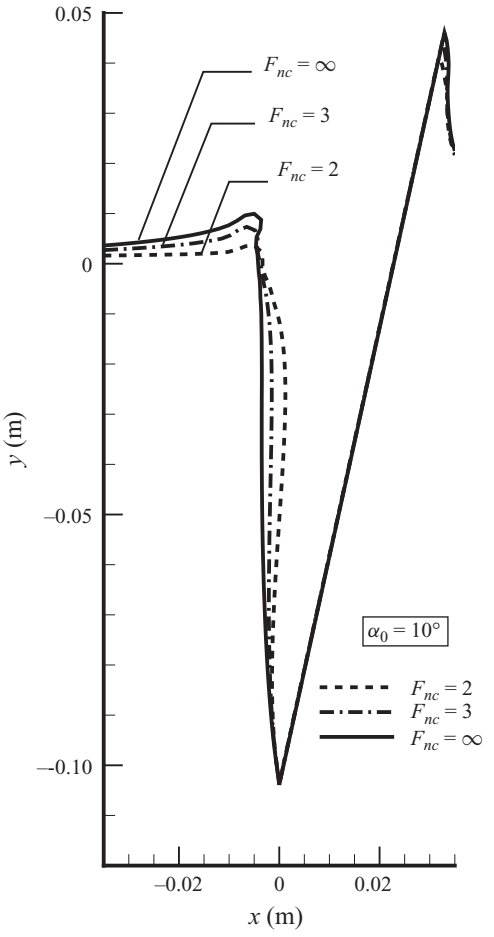

FIGURE 18. Ventilating entry of a surface-piercing hydrofoil: effect of the Froude number on the ventilated-surface shapes. $F_{nc} = \infty$ corresponds to $g = 0$. $V_w = 2.45$ m s^{-1} for $F_{nc} = 2.0$ and $V_w = 3.67$ m s^{-1} for $F_{nc} = 3.0$.

(*a*) All the nonlinearities of the three-way interaction among the hydrofoil, the ventilated surface and the free surface are retained through the use of fully nonlinear free-surface boundary conditions.

(*b*) The scheme can be applied to general hydrofoil shapes and inflow conditions.

(*c*) With gravity taken into consideration, the scheme allows for the effects of having a finite Froude number.

The numerical scheme and the results presented here have been verified via systematic grid-independent studies, and validated through a comparison with previously available experimental and analytical results.

The shortcomings of a linearized free-surface approach have been illustrated by comparing the results of the current method with that of Savineau & Kinnas (1995). In comparison to the nonlinear method, the linear method tends to predict the ventilated surface to be further away from the suction side of the hydrofoil. It also under-predicts the pressure and the total force, especially since it ignores the contribution from the free-surface elevation and jet on the pressure side of the hydrofoil.

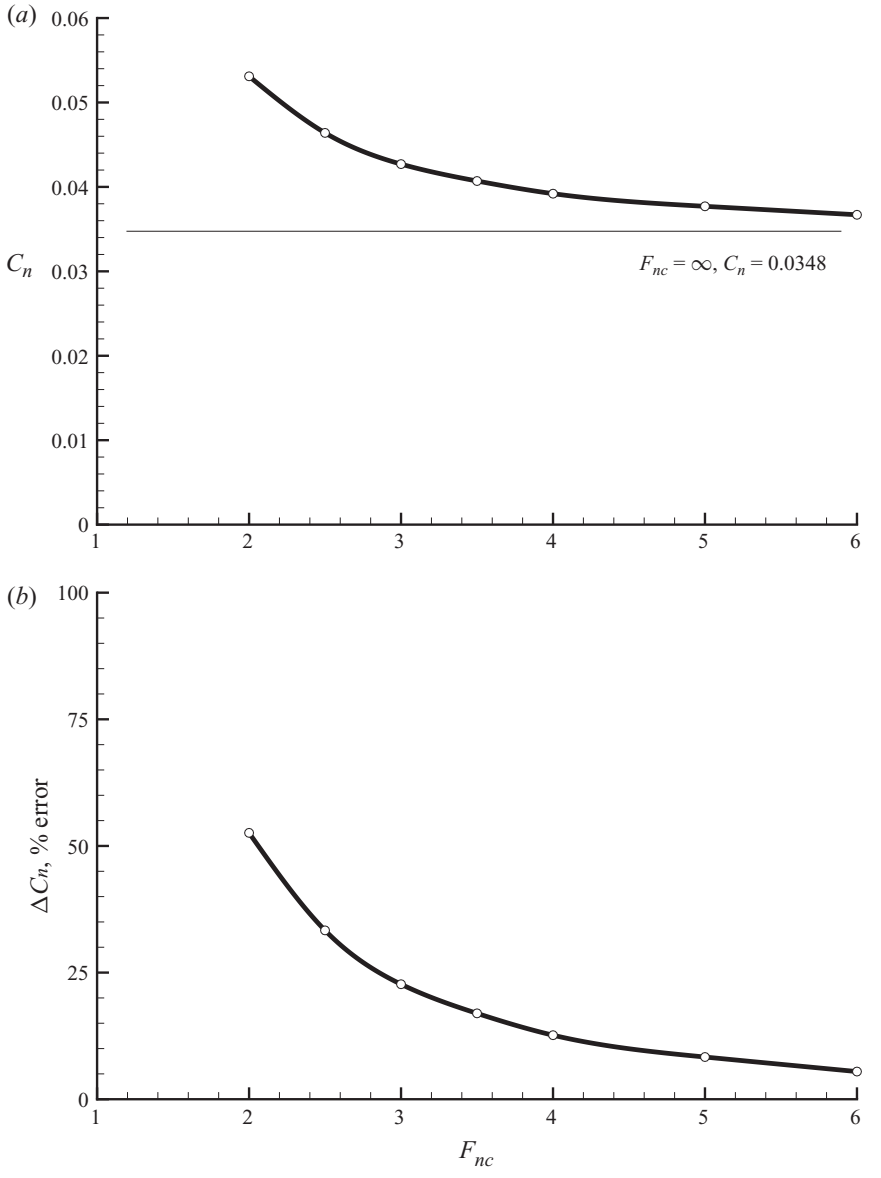

FIGURE 19. Ventilating entry of a surface-piercing hydrofoil: effect of the Froude number on the normal force coefficient. $F_{nc} = \infty$ corresponds to $g = 0$. (*a*) Normal force coefficient, C_n. (*b*) Error in normal force coefficient, $\Delta C_n = (C_n - C_{n\infty})/C_{n\infty} \times 100$, where $C_{n\infty}$ is the normal force corresponding to $F_{nc} = \infty$. Angle of attack $\alpha_0 = 10°$.

In terms of future research directions, the current method can be seen as a precursor to including fully nonlinear free-surface boundary conditions in a three-dimensional scheme for the performance prediction of surface-piercing propellers. A framework to build on is the three-dimensional BEM-based scheme described in detail in Young (2002) and Young & Kinnas (2003), which in itself is an extension of the numerical method developed by Kinnas & Fine (1993) for predicting cavitation on three-dimensional hydrofoils.

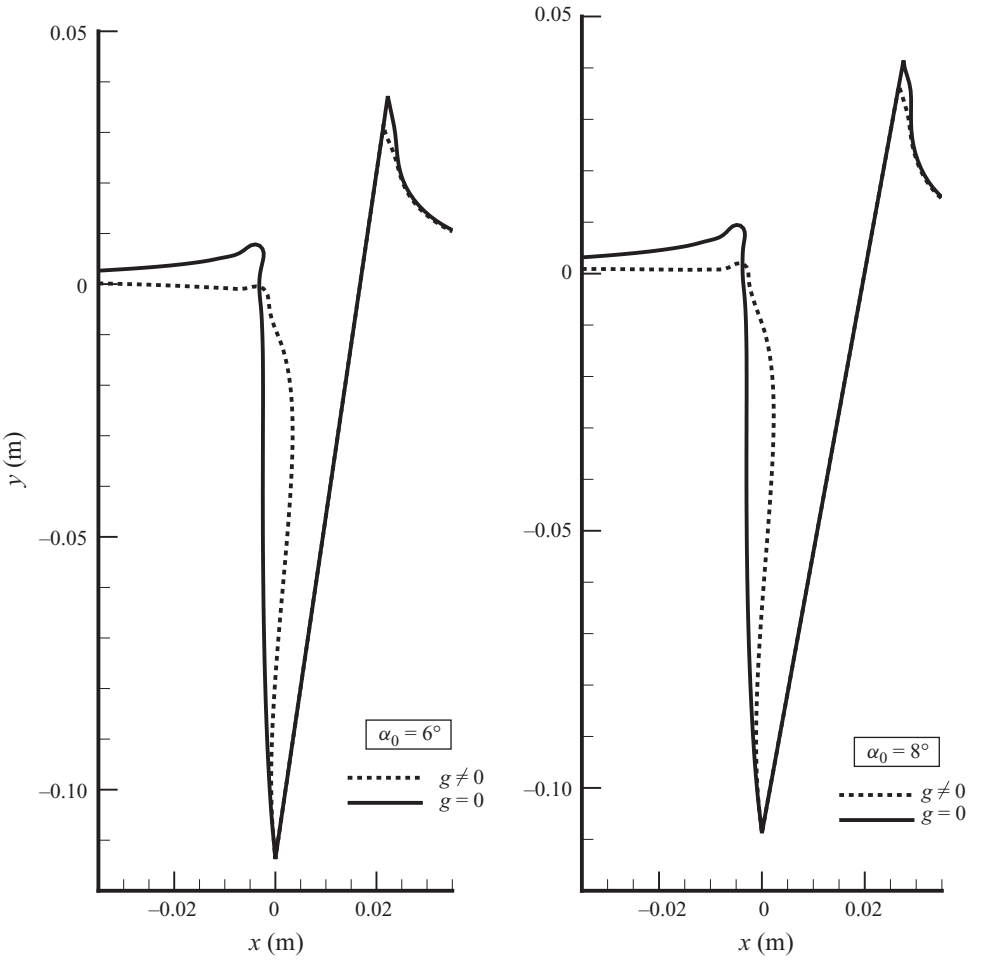

FIGURE 20. Ventilating entry of a surface-piercing hydrofoil: effect of angle of attack on the ventilated-surface shapes with ($g \neq 0$) and without ($g = 0$) the presence of gravity; $g \neq 0$ corresponds to $F_{nc} = 2.0$.

The method of Young & Kinnas (2003) simplifies the performance analysis by using a negative-image method for the free surface. Despite this approximation, the method predicts the mean forces with reasonable accuracy when compared to the experimental results of Olofsson (1996). However, discrepancies are observed in the dynamic behaviour of the forces, especially at the entry stage of the blade cycle and this can be attributed to the lack of nonlinear free-surface effects. The fully nonlinear two-dimensional method presented here can be extended to the three-dimensional scheme to improve the treatment of the free surface. In addition to the nonlinear effects of the free surface, the effect of gravity has to be taken into account to predict the performance characteristics at low speeds of operation and also improve the pressure distribution at the inner radii of the propeller at higher speeds. The authors feel that including fully nonlinear free-surface effects along with the inclusion of gravity should improve the correlation with experiments and also the prediction of performance characteristics over a large range of operating conditions.

Support for this research was provided by the Office of Naval Research (Contract N00014-07-1-0932, Monitor: Ms K. Cooper). The authors wish to thank Dr B. Cox for sharing with them information on his experimental observations. The authors also wish to thank Dr A. Iafrati of INSEAN for his valuable comments regarding the numerical aspects of the water-entry problem.

REFERENCES

Birkhoff, G. & Zarantonello, E. H. 1957 *Jets, Wakes, and Cavities*. Academic.

Chekin, B. S. 1989 The entry of a wedge into an incompressible fluid. *J. Appl. Math. Mech.* **53** (3), 300–307.

Cox, B. D. 1971 Hydrofoil theory for vertical water entry. PhD thesis, Massachusetts Institute of Technology, Cambridge, MA.

Dobrovol'skaya, Z. N. 1969 On some problems of similarity flow of fluid with a free surface. *J. Fluid Mech.* **36** (4), 805–829.

Dussan V., E. B. 1976 On the difference between a bounding surface and a material surface. *J. Fluid Mech.* **75** (4), 609–623.

Faltinsen, O. M. 2005 *Hydrodynamics of High-Speed Marine Vehicles*. Cambridge University Press.

Faltinsen, O. M. & Semenov, Y. A. 2008 Nonlinear problem of flat-plate entry into an incompressible liquid. *J. Fluid Mech.* **611**, 151–173.

Gilbarg, D. 1960 Jets and cavities. *Handbuch Phys.* **9**, 311–445.

Kihara, H. 2006 A computing method for the flow-analysis around a prismatic planing-hull. In *Proceedings of the 5th International Conference on High-Performance Marine Vehicles*, Australia (ed. P. K. Sahoo), pp. 262–272.

Kinnas, S. A. & Fine, N. E. 1993 A numerical nonlinear analysis of the flow around two- and three-dimensional partially cavitating hydrofoils. *J. Fluid Mech.* **254** (1), 151–181.

Longuet-Higgins, M. S. & Cokelet, E. D. 1976 The deformation of steep surface waves on water. I. A numerical method of computation. *Proc. R. Soc. Lond.* A **350**, 1–26.

Olofsson, N. 1996 Force and flow characteristics of a partially submerged propeller. PhD thesis, Department of Naval Architecture and Ocean Engineering, Division of Hydromechanics, Chalmers University of Technology, Gothenburg, Sweden.

Panton, R. L. 1984 *Incompressible Flow*. John Wiley.

Savineau, C. M. & Kinnas, S. A. 1995 A numerical formulation applicable to surface piercing hydrofoils and propellers. In *24th American Towing Tank Conference* (ed. P. Johnson). Texas A&M University.

Shiba, H. 1953 Air-drawing of marine propellers. *Tech. Rep.* 9. Transportation Technical Research Institute, Tokyo, Japan.

Sun, H. & Faltinsen, O. M. 2007 The influence of gravity on the performance of planing vessels in calm water. *J. Engng Math.* **58** (1), 91–107.

Terent'ev, A. G. 1979 Inclined entry of a thin body with ventilated cavity into an ideal imponderable liquid. *Fluid Dyn.* **14** (3), 377–385.

Vinayan, V. 2009 A boundary element method for the strongly nonlinear analysis of ventilating water-entry and wave-body interaction problems. *UT-OE Rep.* 09-2. PhD thesis, Ocean Engineering Group, Department of Civil Engineering, Architectural and Environmental Engineering, University of Texas at Austin, Austin, TX.

Vinayan, V. & Kinnas, S. A. 2008 Numerical modeling of surface piercing hydrofoils and propellers. In *Proceedings of the 27th Symposium on Naval Hydrodynamics, Seoul, Korea.* Office of Naval Research.

Wang, D. P. 1977 Water entry and exit of a fully ventilated foil. *J. Ship Res.* **21** (1), 44–68.

Wang, D. P. 1979 Oblique water entry and exit of a fully ventilated foil. *J. Ship Res.* **23** (1), 43–54.

Wehausen, J. V. & Laitone, E. V. 1960 Surface waves. *Handbuch Phys.* **9** (3), 446–778.

Wu, T. Y. T. 1955 A free streamline theory for two-dimensional fully cavitated hydrofoils. *Tech. Rep.* 21–17. California Institute of Technology, Pasadena, CA.

Yim, B. 1969 An application of linearized theory to water entry and water exit problems. Part 2. With ventilation. *Rep.* 3171. NSRDC, Washington, DC.

Yim, B. 1971 Investigation of gravity and ventilation effects in water entry of thin foils. In *Proceedings of the IUTAM Symposium on Nonsteady Flows of Water with High Velocities* (ed. L. I. Sedov & G. Yu. Stepanov), pp. 471–489. Nauka.

Yim, B. 1974 Linear theory on water entry and exit problems of a ventilating thin wedge. *J. Ship Res.* **18** (1), 1–11.

Young, Y. L. 2002 Numerical modeling of supercavitating and surface-piercing propellers. *UT-OE Rep.* 02-1. PhD thesis, Ocean Engineering Group, Department of Civil, Architectural and Environmental Engineering, University of Texas at Austin, Austin, TX.

Young, Y. L. & Kinnas, S. A. 2003 Numerical modeling of supercavitating propeller flows. *J. Ship Res.* **47** (1), 48–62.

Zhao, R. & Faltinsen, O. 1993 Water entry of two-dimensional bodies. *J. Fluid Mech.* **246**, 593–612.

Zhao, R., Faltinsen, O. M. & Aarsnes, J. 1996 Water entry of arbitrary two-dimensional sections with and without flow separation. In *Proceedings of the 21st Symposium on Naval Hydrodynamics*, pp. 408–423. National Academy Press.